Energy Storage Materials 15 (2018) 108–115

Contents lists available at ScienceDirect

Energy Storage Materials

journal homepage: www.elsevier.com/locate/ensm

Superior Na-ion storage achieved by Ti substitution in $Na_3V_2(PO_4)_3$

Yangyang Huang[a], Xiang Li[a,1], Jinsong Wang[b], Lin Miao[b], Chang Li[a], Jiantao Han[a,*], Yunhui Huang[a,*]

[a] State Key Laboratory of Material Processing and Die & Mould Technology, School of Materials Science and Engineering, Huazhong University of Science and Technology, Wuhan, Hubei 430074, China

[b] Wuhan National Laboratory for Optoelectronics, and School of Optical and Electronic Information, Huazhong University of Science and Technology, Wuhan 430074, China

ARTICLE INFO

Keywords:
Sodium-ion batteries
Cathode
Ti-Substitution
Superior performance
X-ray pair distribution function

ABSTRACT

The development of sodium-ion batteries (SIBs) remains a great challenge due to poor stability and sluggish kinetics of cathode materials. Here, we present Ti-substituted $Na_{3-x}V_{2-x}Ti_x(PO_4)_3$/C (NVP-$Ti_x$/C , $0 \le x \le 0.2$) as high-performance cathode materials for SIBs. Crystal structure and Na storage properties are investigated by experiment and theoretical calculation. X-ray diffraction results reveal that NVP-Ti_x have same rhombohedral structure as NVP but shrunk lattice parameters. Pair distribution function spectra and the calculated crystal structure suggest that the local structural distortion of the doped samples originates from slight decrease of V–O bond. As SIB cathode materials, greatly enhanced structural stability and electrochemical performance are achieved by Ti substitution. Especially, NVP-$Ti_{0.15}$/C exhibits excellent rate capability and cyclability with capacity retention of 60% after 2000 cycles at high rate of 10 C. Importantly, even at 20 C, a reversible capacity of 63 mAh g^{-1} is maintained after 300 cycles at elevated temperature of 60 °C. Density functional theory calculations demonstrate that the superior electrochemical performance of the Ti-doped samples can be attributed to the enhanced intrinsic electronic conductivity, low Na^+ diffusion energy barrier and high structural stability.

1. Introduction

In recent years, due to natural abundance and low cost of sodium, an increasing attention has been paid to sodium-ion batteries (SIBs), the promising alternatives to lithium-ion batteries for the potential application especially in large-scale energy storage [1–6]. However, the ionic radius of Na ion is far larger than Li ion, resulting in much lower rate capability and poorer cycle life for SIBs as compared with the lithium counterparts. The larger Na^+ radius severely restricts the diffusion kinetics of Na^+ ions in host materials, especially in cathode materials [7–10]. Therefore, improving Na^+ diffusion kinetics of is crucial for developing high-performance electrode materials for SIBs.

Recently, plenty of layered transition oxides have been studied as the promising candidates of electrode materials for SIBs to pursue reversible and rapid Na-ions insertion/extraction [11–16]. However, the low intrinsic electrical conductivity, irreversible phase transition and Na-ion storage instability greatly affect the electrochemical performance. Compared with oxides, polyanionic phosphate $Na_3V_2(PO_4)_3$ (NVP) shows open 3D host frameworks and large tunnels for Na^+ migration, resulting in good stability and safety [17–22]. However, the intrinsic poor electronic conductivity leads to poor cycle life and rate capability, which seriously hinders the practical application. To date, there are three major methods to overcome these fundamental shortcomings: coating with various carbon materials, reducing the particle size to the nanoscale, and doping with foreign ions [23–27]. In general, the electric conductivity of NVP can be improved by carbon coating, while the ionic conductivity can be enhanced by decreasing particle size due to shortened Na-ion diffusion distance. However, it is difficult for NVP to change the intrinsic characteristics by these methods.

Cationic doping is considered as an effective strategy to improve the intrinsic properties. Various metallic ions with different valences and ionic sizes (such as Cr^{3+}, Fe^{2+}, K^+, etc.) have been employed to partially substitute V or Na in NVP to achieve high capacity and excellent rate capability. When doping cations with higher valence than V^{3+} are used to substitute in NVP, Na^+ vacancies might be formed for valence balance, which are favorable for the diffusion of Na ions [28]. Since the ionic radius of Ti^{4+} (0.064 nm) is smaller than that of V^{3+} (0.074 nm) and TiO_6 octahedral is more stable than VO_6 octahedral, Ti^{4+} is often

* Corresponding authors.
E-mail addresses: jthan@hust.edu.cn (J. Han), huangyh@hust.edu.cn (Y. Huang).
[1] Xiang Li contributed equally to this work.

https://doi.org/10.1016/j.ensm.2018.03.021
Received 29 December 2017; Received in revised form 7 March 2018; Accepted 25 March 2018
Available online 27 March 2018
2405-8297/ © 2018 Elsevier B.V. All rights reserved.

chosen as a dopant for V-containing materials [29,30]. It has been recognized that Ti doping is helpful to increase the electrical conductivity, suppress phase transition and stabilize the structure.

To the best of our knowledge, there is no report on the effect of Ti substitution on the performance of NVP. We herein present Ti-substituted $Na_{3-x}V_{2-x}Ti_x(PO_4)_3$/C (NVP-$Ti_x$/C, $0 \le x \le 0.2$) as cathode materials for SIBs. The effects of Ti substitution on crystal structure, reaction kinetics and Na-ion diffusion have been demonstrated by experimental and theoretical studies. By optimizing the electrochemical properties of NVP-Ti_x/C, we find that NVP-$Ti_{0.15}$/C exhibits the best cyclability, rate capability and Na-ion diffusion kinetics. Operando X-ray diffraction (XRD) patterns reveal that the Ti-substituted samples undergo small volume change during insertion/extraction process, indicative of stable structure. Density functional theory (DFT) calculations indicate that the improved Na^+ migration derives from enhanced intrinsic electronic conductivity, low Na^+ diffusion energy barrier and high structure stability.

2. Experimental section

2.1. Materials synthesis

A series of NVP-Ti_x/C ($0 \le x \le 0.2$) samples were synthesized through a facile one-step solid-state method with Na_2CO_3, $NH_4H_2PO_4$, V_2O_5, TiO_2 and glucose as raw materials. Glucose served as carbon source. The weight ratio of glucose to other raw materials was 6: 100. Stoichiometric raw materials were put into a nylon jar with 10 mL ethanol. The mixture was high-energy ball milled for 30 min before being dried at 80 °C for 10 h. Finally, the dried precursor was sintered at 800 °C for 10 h in 5% H_2/Ar atmosphere to obtain pure NVP-Ti_x/C ($0 \le x \le 0.2$) samples.

2.2. Materials Characterization

The *in-situ* XRD patterns of the electrode materials during cycling were collected on a PANalytical Empyrean diffractometer equipped with a Cu Kα radiation. The phase of the as-prepared samples was confirmed by Rietveld refinement with General Structure Analysis System (GSAS) [31]. The pair distribution function (PDF) data were obtained on a PANalytical Empyrean outfitted with Ag K_α radiation and Rh K_β filter detector. The total collection time of PDF data was 6.8 h for each sample. The data conversion was performed on Highscore software provided by PANalytical Corporation. The morphology of samples was observed by scanning electron microscope (SEM, FEI Nova NanoSEM 450). Elemental analysis was conducted on an energy-dispersive X-ray spectroscopy (EDS) device attached to SEM equipment. The microstructure was obtained using a high-resolution transmission electron microscope (HR-TEM, JEOL JEM-2100). The oxidation state of V was investigated by X-ray photoelectron spectroscopy (XPS, AXIS-ULTRA DLD-600W). The carbon coating on samples was verified by Raman spectroscopy with an operating power level of 2 mW on a confocal Raman spectrometer (Thermfisher US).

2.3. Electrochemical tests

The electrochemical measurements were carried out with 2032 coin cells assembled in an argon-filled glove box. The cathode electrodes were prepared by pasting a slurry containing active material, super P and poly(vinyl difluoride) (PVDF) (7: 2: 1 by weight) coating onto Al foil substrate and dried at 120 °C for 12 h under vacuum. The mass loading of the electrode was around 2.1 mg cm^{-2}. 1.0 mol L^{-1} $NaClO_4$ in propylene carbonate (PC) with 2 vol% 4-fluoro-1,3-dioxolan-2-one (FEC) additive was adopted as electrolyte. Sodium metal foil was used as counter electrode. The separator was made from glass fiber membrane (Whatman). Galvanostatic charge/discharge was performed on LAND battery system (CT2001A, Wuhan, China) within a voltage range of 2.3 – 3.9 V *vs.* Na/Na^+ at 25 °C and 60 °C. Electrochemical impedance spectroscopy (EIS) was measured on an electrochemical workstation (Princeton, USA) over a frequency range from 100 kHz to 10 MHz with an applied amplitude of 5 mV.

2.4. Computation methods

First-principles calculations were performed based on density functional theory (DFT) with Vienna *ab* initio simulation package (VASP) [32,33]. The interaction between core ion and valence electron was described by the projector augmented wave method (PAW) [34]. The exchange-correlation function was calculated using generalized gradient approximation (GGA) described by the Perdew, Burke, and Ernzerhof (PBE) with Hubbard *U* corrections [35,36]. The value of U = 4.2 eV was used for Coulomb corrections to the *d* states on the basis of previous work in cobalt oxides [28]. An energy cutoff of 500 eV was used with Monkhorst *k*-points sampling scheme (4×4×2 for geometry optimization, while a larger grid 8×8×4 was used for electronic structure computation [37]. Conjugated gradient method was employed to the geometry optimization and all the atomic coordinates were fully relaxed till the maximal force on each atom was less than 0.02 eV $Å^{-1}$, and the convergence condition for energy was 10^{-4} eV. The Na^+ migration pathway and the corresponding energy barrier were optimized with the nudged elastic band (NEB) method [38].

3. Results and discussion

Phase analysis of NVP-Ti_x/C was confirmed by XRD patterns, as plotted in Fig. 1a. All diffraction peaks can be assigned to a rhombohedral NASICON structure with *R*−3*c* space group, agreeing well with the previous report [39]. No impurity phase is detected, indicating that the substitution of Ti in NVP/C does not alter the pristine structure. XPS further confirms that there is no obvious change in the oxidation states of both V and Ti in NVP-Ti_x/C. Figs. 1b and 1c, as well as Figure S1 display the high-resolution XPS spectra of V 2p and Ti 2p of NVP-$Ti_{0.15}$/C and NVP/C. The peaks of binding energy at 517.2 and 524.1 eV correspond to $2p_{3/2}$ and V $2p_{1/2}$ of V^{3+}, respectively [40]. There are no higher binding energies near 519–520 eV belonging to V^{4+} or V^{5+} for the Ti-doped samples. It can be concluded that Ti ions are successfully doped into the structure of NVP/C without forming other phases.

The SEM images of NVP-Ti_x/C (Figure S2) show irregular morphologies with inhomogeneous particle size. EDS mapping illustrates that Ti element is uniformly distributed in each particle without segregation (Figure S3). HR-TEM images (Figure S4) of NVP/C and NVP-$Ti_{0.15}$/C demonstrate that the particles are coated by carbon layer with a thickness of around 2 nm. Interplanar spacings of 0.62 and 0.40 nm correspond to the (012) and (104) planes of NVP/C and NVP-$Ti_{0.15}$/C, respectively. The Raman Gaussian numerical simulation spectra are shown in Figures S4c and S4f. The fitted peak 2 at 1360 cm^{-1} and peak 4 at 1600 cm^{-1} are related to sp^2 type carbon while peak 1 at 1200 cm^{-1} and peak 3 at 1530 cm^{-1} can be assigned to sp^3 type carbon. The area ratio between sp^3 and sp^2 ($A_{sp}{}^3/A_{sp}{}^2$) can be used to verify the structural characteristic of the carbon layer [41]. The calculated $A_{sp}{}^3/A_{sp}{}^2$ values are 0.48 and 0.42 for NVP/C and NVP-$Ti_{0.15}$/C, respectively, suggesting that a large amount of coated carbon in both samples exist in sp^2 type. As seen in Figure S5, both of NVP-Ti_x/C ($0 \le x \le 0.2$) contain a small amount of carbon, and the carbon layer plays role in both samples for the electrochemical properties is similar.

In order to understand the structural change induced by Ti substitution at V sites, Rietveld refinement was conducted for NVP-Ti_x/C (Fig. 1d and S6). Based on the XRD refinement, the changes of lattice parameters and sodium occupancy with Ti content are presented in Fig. 2a–c. With increasing Ti content, the lattice parameters *a*, *c* and *V* decrease obviously, which is because the radius of Ti^{4+} is smaller than that of V^{3+}. The occupancies of Na1 and Na2 sites dependent on Ti

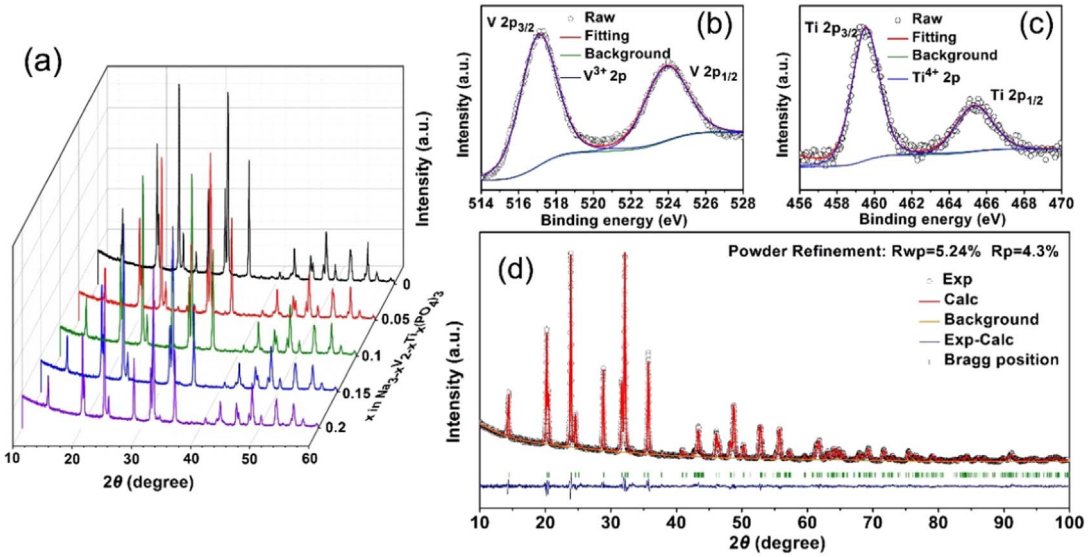


Fig. 1. (a) XRD patterns of NVP-Ti_x/C ($0 \le x \le 0.2$). (b, c) High-resolution XPS of V2p and Ti2p for NVP-$Ti_{0.15}$/C. (d) Rietveld refined XRD patterns of NVP-$Ti_{0.15}$/C.

substitution are plotted in Fig. 2d. The occupancy at Na1 site increases slightly whereas the occupancy at Na2 site decreases with increasing Ti content, resulting in more vacancies at Na2 sites. The polaron would form at the first nearest-neighbor V site to the Na vacancy when Na vacancy is introduced [28]. Diffusion of Na ions was treated as a process of the polaron–Na vacancy complexes. Fig. 2e–f display the rhombohedral NASCON structure and hexagonal bottlenecks of NVP/C. The NASCON structure is a three-dimensional framework built from $[V_2(PO_4)_3]$ units formed by corner-sharing of VO_6 octahedra and PO_4 tetrahedra along *c*-axis direction (Fig. 2e). Corner-sharing of three VO_6 octahedra and three PO_4 tetrahedra forms the hexagonal bottlenecks with short diameter of 4.74 Å (Fig. 2f). Na ions can diffuse in the large interstitial sites provided by these hexagonal bottlenecks. The bond lengths obtained from the refinement are listed in Table S1. The average lengths of V–O and P–O bonds for NVP-$Ti_{0.15}$/C are shorter than those for NVP/C, indicating that the structure becomes more stable by Ti substitution. Na ions diffusion in the hexagonal bottlenecks for NVP-$Ti_{0.15}$/C are much easier than that of NVP/C. Moreover, the average length of Na–O bond in NVP-$Ti_{0.15}$/C is longer than in NVP/C. A longer Na–O bond has a smaller binding energy, leading to an easier migration of Na^+ due to the reduction of the energy barrier. Thus the longer Na–O bond is beneficial to the electrochemical performance of embedded materials especially at high current density [42].

To further explore the effect of Ti substitution in NVP/C, the X-ray pair distribution function (PDF) analysis was introduced to gain local structural insight. This powerful method has been successfully used to understand the behavior of cathode materials [43,44]. The PDF curves of NVP/C and NVP-$Ti_{0.15}$/C are plotted in Fig. 2g (0.5–6 Å)

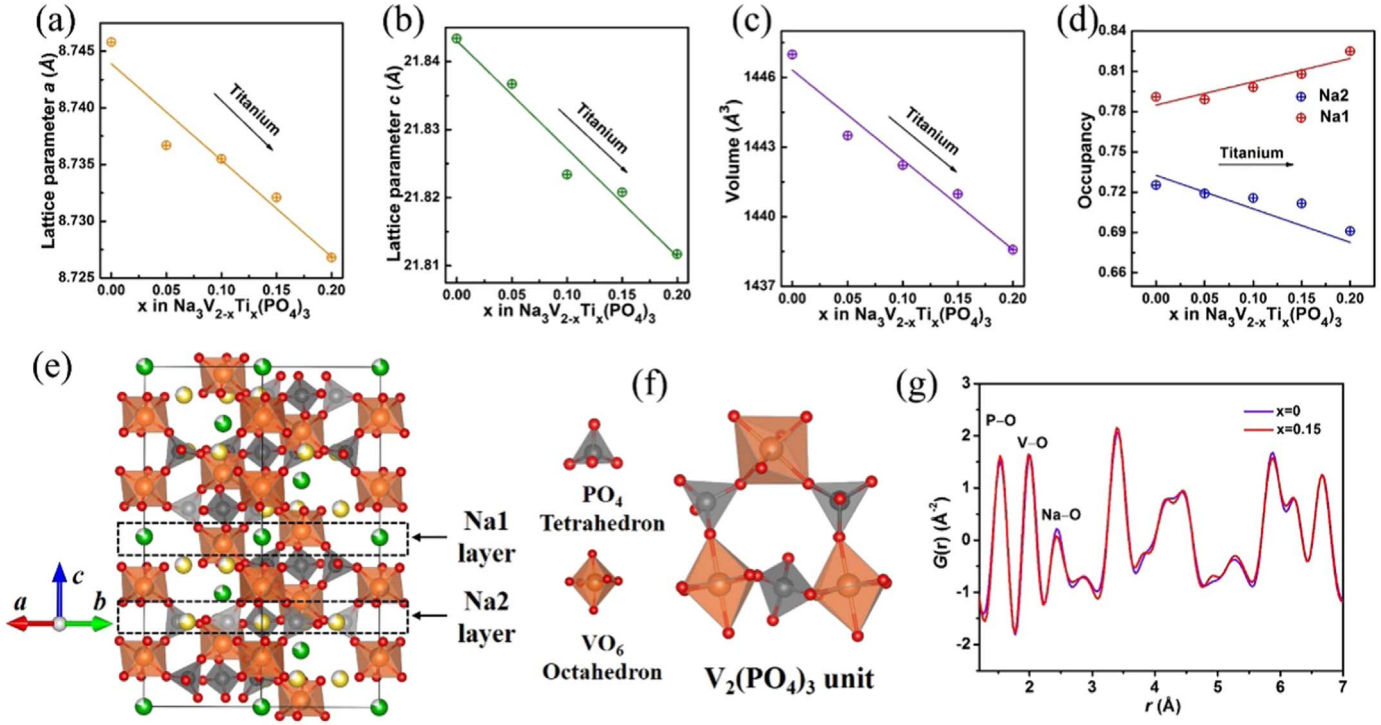


Fig. 2. Dependence of (a–c) lattice parameters (*a*, *c* and *V*) and (d) occupancy of Na1 and Na2 on *x* for NVP-Ti_x/C ($0 \le x \le 0.2$) based on Rietveld refinement. (e) Crystal structure: V and Ti ions are shown in red, VO_6 appears as octahedra. (f) The Na-ion migration channel. (i) The PDF profiles of NVP-$Ti_{0.15}$/C and NVP within 7 Å.

and Figure S7 (0.5–50 Å). The atomic PDF (Fig. 1c) for both samples shows a series of sharp peaks, each of which corresponds to an interatomic distance.

As expected, the PDF curve of the doped sample (Figure S7) shows similarity with the pristine material, which indicates that Ti doping would not significantly change the structure of NVP/C. The slight difference in peak position and intensity between undoped and doped NVP/C indicates little local structure change (*e.g.* disordered extent, vacancies, etc.). In particular, the peaks locate below 2.1 Å related to the P–O and V–O pairs show a slight contraction as the titanium introduced, causing broadening of the channels for Na ion diffusion. The third peak relates to Na–O correlations, whose intensity of Ti substitution sample is lower than that of the pristine sample, indicating a higher concentration of sodium vacancies in Ti substitution sample. Moreover, the decrease in intensity of this peak is direct evidence of Ti doping in V site.

Cyclic voltammetry (CV) and galvanostatic intermittent titration technique (GITT) were employed to observe the effect of Ti substitution on the reaction kinetics and voltage hysteresis between charge and discharge profiles. We compared the sodium storage performances for NVP/C and NVP-$Ti_{0.15}$/C. CV curves at a scan rate of 0.1 mV s^{-1} (Fig. 3a) exhibit a couple of redox peaks from V^{3+} to V^{4+} [45]. NVP/C shows a potential interval of ~ 37 mV, whereas the NVP-$Ti_{0.15}$/C show much smaller intervals. Moreover, the redox peak profile of NVP-$Ti_{0.15}$/C is more symmetric and sharper than that of NVP/C, which suggests that the redox kinetics is enhanced due to the improvement of conductivity and the reduced activation energy [46]. In general, GITT is designed for studying chemical diffusion coefficient in solid solution systems, but it can provide comparative information on the electrode kinetics of a two-phase system through analyzing the voltage relaxation time to equilibrium potential and the magnitude of overpotential. As shown in Fig. 3b, NVP/C shows an equilibrium voltage gap of about 20 mV after relaxation, which is twice than that of NVP-$Ti_{0.15}$/C (*ca.* 10 mV). The substituted electrode also exhibits a narrower equilibrium potential hysteresis than the pristine electrode. Lower overpotential and reduced polarization indicate that the Ti substituted sample has much faster kinetics than the pristine NVP/C [47,48].

Fig. 3c shows the initial charge/discharge profiles of NVP-Ti_x/C ($0 \le x \le 0.2$) in voltage range from 2.3 to 3.9 V at 1 C (1 C = 117 mA g^{-1}). All curves display flat charge and discharge plateaus at around 3.4 and

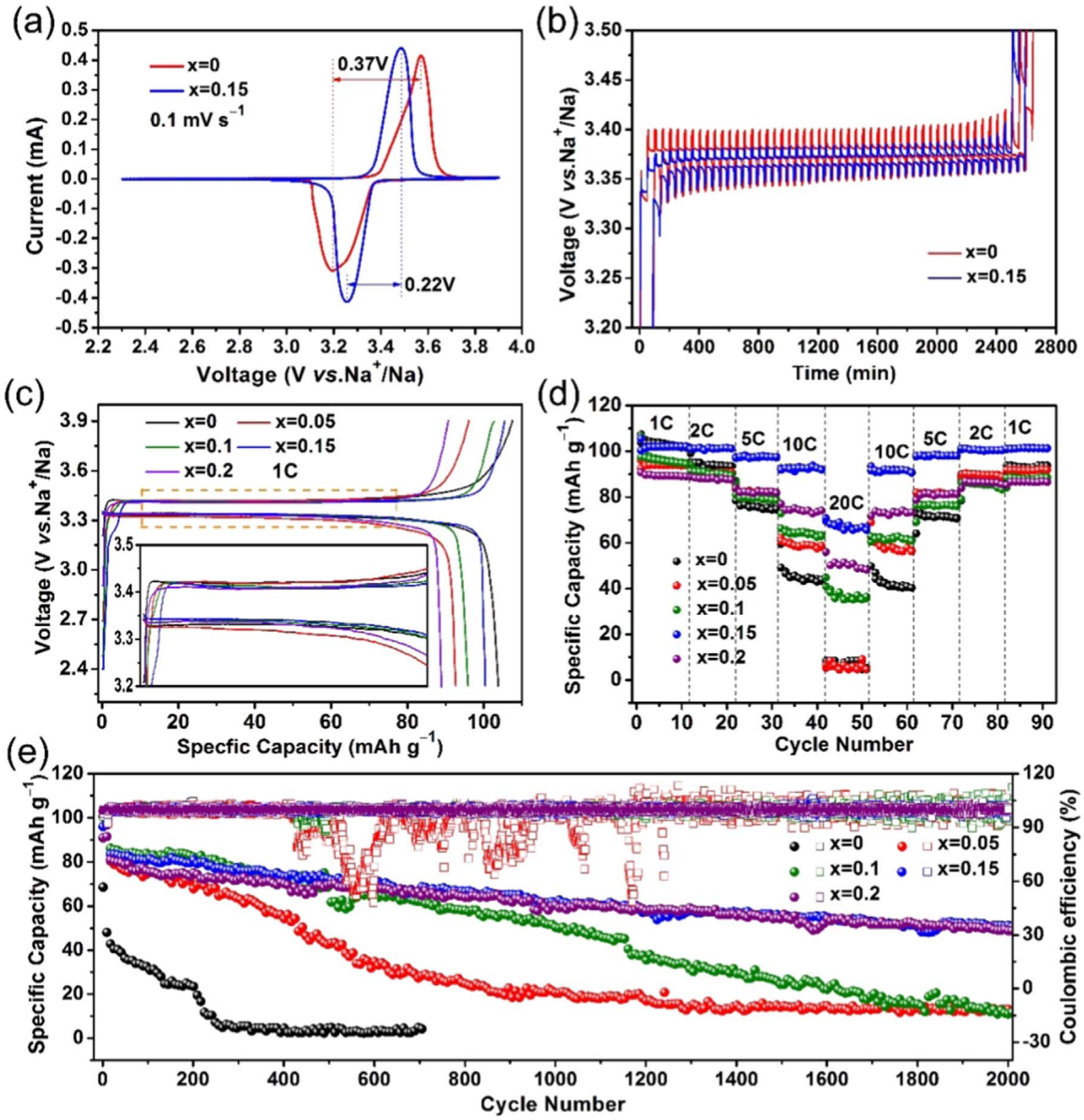


Fig. 3. (a) CV curves of NVP-$Ti_{0.15}$/C and NVP/C electrode. (b) GITT experiment at 0.05 C for 1 h followed by 4 h relaxation. (c) Charge-discharge profiles of NVP-Ti_x/C ($0 \le x \le 0.2$) electrodes. (d) Capacity of NVP-Ti_x/C ($0 \le x \le 0.2$) at various rates. (e) Long-term cycling stability of NVP-Ti_x/C ($0 \le x \le 0.2$).

3.35 V, corresponding to the redox couple of V^{3+}/V^{4+} [49]. Compared with pristine NVP/C, Ti-doped NVP-Ti$_x$/C electrode deliver lower initial specific discharge capacity. The decreased capacity may result from the substitution of inactive element Ti for V. Besides, replacing V^{3+} with Ti^{4+} reduces Na content in NVP/C. From the inset in Fig. 3c, the gap between charge and discharge of NVP-Ti$_{0.15}$/C is the narrowest, suggesting that it has the lowest overall resistance and the fastest kinetics. Rate performance measurements at current densities from 1 to 20 C were conducted to investigate the effect of Ti substitution on rate performance, as shown in Fig. 3d. It is apparent that all doped samples deliver better rate performances than pristine one. And it is noted that the substituting level of Ti has a significant impact on the rate performance. Obviously, NVP-Ti$_{0.15}$/C shows the best rate capability among various NVP-Ti$_x$/C electrodes. All samples do not show a clear difference in specific capacity when charged/discharged at 1 C, but NVP-Ti$_{0.15}$/C electrode exhibits remarkably enhanced electrochemical performance at high current densities. NVP/C displays a discharge capacity of 95.2, 78.4, 49.1 and 8.5 mAh g^{-1} at rates of 2, 5, 10 and 20 C, respectively. In contrast, NVP-Ti$_{0.15}$/C shows remarkably enhanced rate capability and delivers a discharge capacity of 101.5, 97.5, 92.6 and 70.8 mAh g^{-1} at 2, 5, 10 and 20 C, respectively. Moreover, it can maintain 70% of initial capacity even at a very high rate of 20 C. When the current density turns back from 20 C to 1 C, it can recover the capacity up to 106.5 mAh g^{-1}, indicative of excellent reversibility. In comparison, NVP/C delivers an extremely low discharge capacity of only 8.5 mAh g^{-1} at 20 C, almost no charge/discharge ability. Therefore, it can be concluded that the rate capability of NVP/C, particularly at high rates, can be significantly improved through Ti substituting. At same rate, with increasing Ti substituting level x, the discharge capacity of NVP-Ti$_x$/C first increases, reaches the maximum value at x = 0.15, and then decreases with further increasing x.

Cyclic stability is an important factor for application of SIBs. A comparison in discharge capacity during cycling for NVP-Ti$_x$/C ($0 \le x \le 0.2$) is presented in Fig. 3e. We can see that Ti-substituted NVP/C materials exhibit better long-term cycle stability than the pristine one at 10 C. NVP-Ti$_{0.15}$/C shows the best cycle performance at 10 C: the capacity is 86 mAh g^{-1} at first cycle and keeps to 60% retention of 51.3 mAh g^{-1} after 2000 cycles. As a comparison, NVP/C delivers an initial capacity of 50 mAh g^{-1} and lost the cycle ability after 200 cycles. For NVP-Ti$_{0.15}$/C, even at 20 C, it still exhibits a capacity as high as 78 mAh g^{-1} and keeps 58% of its initial capacity after 1200 cycles (Figure S8). Moreover, its Coulombic efficiency is almost 100% throughout the cycling. The chart of Fig. 3 indicates that the stabilization effect of Ti substituting is spectacular and obvious. Such excellent rate capability and cyclic stability are quite impressive when compared to results from the reported literature (Table S2).

The electrochemical performance of NVP-Ti$_x$/C ($0 \le x \le 0.2$) electrodes was also investigated at relatively high temperature of 60 °C (Fig. 4). Fig. 4a exhibits rate performance of NVP-Ti$_x$/C ($0 \le x \le 0.2$) electrodes at current rates from 2 C to 20 C. It is clear that the rate capability of all substituted samples is better than that of pristine NVP/C, especially at high current densities. The capacities for all electrodes do not show a clear difference at 2 C and 5 C, but NVP-Ti$_{0.15}$/C electrode exhibits remarkably improved electrochemical property when tested at higher current density. The capacity of NVP-Ti$_{0.15}$/C is 101.2 and 81.6 mAh g^{-1} at 10 C and 20 C, respectively. However, NVP/C electrode delivers only the capacity of 40 mAh g^{-1} at 10 C and has lost the ability to charge/discharge at 20 C. It can be concluded that Ti substituting can improve both the specific capacity and rate performance, especially at high current density. The charge/discharge profiles of NVP-Ti$_{0.15}$/C and NVP/C at various high rates are presented in Fig. 4b and Figure S9. It can be seen that with increasing current density, the voltage gap between the charge and discharge plateau increases for both samples. NVP-Ti$_{0.15}$/C exhibits a more smooth voltage plateau and a narrower voltage gap between the charge and discharge profile compared to NVP/C, further indicating that the kinetics of electrochemical reaction at high temperature are improved by Ti substitution on V. At current rate higher than 10 C, NVP-Ti$_{0.15}$/C delivers a pair of apparent charge/discharge plateaus. Whereas, NVP/C shows declined slopes at rates higher than 5 C. The cycling stability of NVP-Ti$_x$/C ($0 \le x \le 0.2$) electrodes at high temperature are displayed in Fig. 4c. The cycling stability of all doped materials is obviously better than the pristine one at high rates, indicating that the cycling performance is enhanced by Ti substitution. It is easy to find out that NVP-Ti$_{0.15}$/C exhibits the best cyclability at 10 C. NVP-Ti$_{0.15}$/C delivers initial specific capacity of 93 mAh g^{-1} and maintains ~ 80 mAh g^{-1} after 500 cycles, indicating only 14% capacity lost. Even at very high rate of 20 C (Fig. 4d), it still exhibits excellent cyclability with only 21% loss over 300 cycles. However, NVP/C only delivers initial capacity of 50 mAh g^{-1} and loses cycle capability after 25 cycles.

The CV curves of NVP/C and NVP-Ti$_{0.15}$/C at various scan rates are shown in Figure S10. With increasing scan rate from 0.1 to 1 mV s^{-1}, NVP-Ti$_{0.15}$/C exhibits smaller potential polarization between oxidation and reduction peaks than NVP/C at same rate, indicative of weaker electrode polarization and faster ionic migration. In Figure S11, the peak current shows a linear relationship with the square root of scan rate for NVP/C and NVP-Ti$_{0.15}$/C. Diffusion coefficient of Na ions (D_{Na}) can be calculated from the slope of the line using Randles-Sevcik equation:

$$i_p/m = 0.4463(F^3/RT)^{1/2} n^{3/2} A D^{1/2} C_0 v^{1/2}$$

The slope from the fitting result for NVP-Ti$_{0.15}$/C is higher than that of NVP/C, indicating that the D_{Na} of the former is higher than that of the latter during sodiation/desodiation process. Faster kinetics can be contributed to the enhanced ionic and electronic conductivities due to Ti substitution.

EIS is a very useful electroanalytical technique for evaluating kinetic and interfacial parameters such as charge-transfer (R_{ct}), double-layer capacitance (C_{d1}) and surface film capacitance (C_f). Figure S12 shows Nyquist plots tested at full desodiation state for NVP/C and NVP-Ti$_{0.15}$/C electrode after different cycles at 10 C. The R_{ct} of the former is smaller than that of the latter, which indicates that the Ti substituting has a surface effect, namely, the increased charge transfer rate and rapid Na ions diffusion through the electrode-electrolyte interface. When tested at fully desodiation state after different cycles at 10 C, it can be observed that R_{ct} decreases due to the activation effect after initial cycle. Subsequently, R_{ct} of NVP-Ti$_{0.15}$/C tends to stabilize throughout 600 cycles, indicative a superior high-rate electrochemical performance. The R_{ct} of NVP/C is unstable after 600 cycles. For NVP-Ti$_{0.15}$/C, the stable R_{ct} during cycling indicates a good long-term cycling stability, which is highly potential for practical application.

Operando XRD technique was employed to investigate the effect of Ti substituing on insertion/extraction mechanism. Fig. 5 and S13 shows the contour plots of operando XRD patterns for NVP-Ti$_{0.15}$/C and NVP/C collected at different states during initial desodiation/sodiation process within a voltage range of 2.3 – 3.9 V at 0.1 C. At the beginning of charging, all diffraction peaks are indexed to NASCON structure, except for the peak of binder. During Na^+ extraction process, all peaks shift to higher angles and some new peaks appear. The new peaks can be indexed to $NaV_2(PO_4)_3$ [17,50]. The intensities of these new peaks increase while those of $Na_3V_2(PO_4)_3$ decrease with continuous charging. The two phases coexist when charging at plateau ~ 3.4 V, but the peak intensity of $Na_3V_2(PO_4)_3$ gradually decreases with further charging, indicating a typical two-phase transfer between $Na_3V_2(PO_4)_3$ and $NaV_2(PO_4)_3$. When the charging is ended at 3.9 V, all peaks can be well indexed to $NaV_2(PO_4)_3$ phase. During discharging, the peaks of $Na_3V_2(PO_4)_3$ appear again and coexist with $NaV_2(PO_4)_3$ till discharging to 2.3 V, in which all peaks are indexed to $Na_3V_2(PO_4)_3$. This means that the material completely transforms back to NASCON

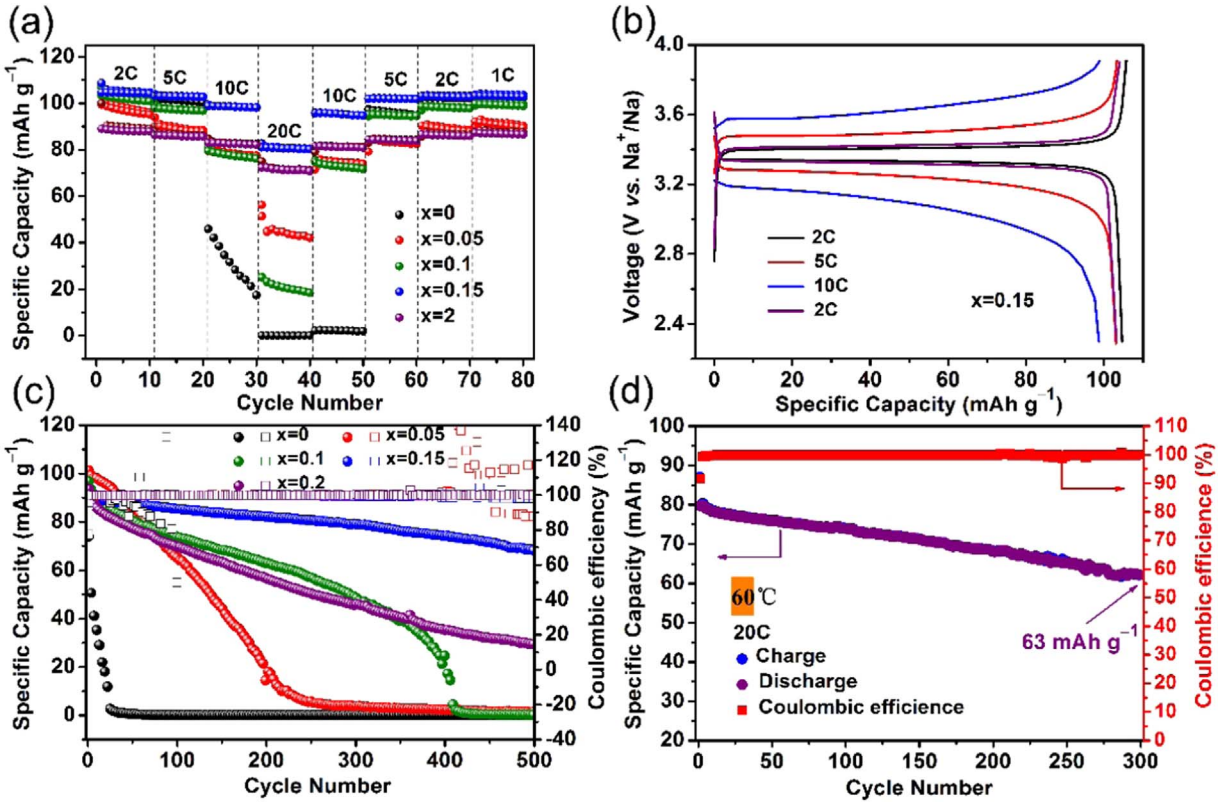


Fig. 4. The electrochemical characterization of NVP-Ti$_x$/C ($0 \le x \le 0.2$) measured at high temperature: (a) Rate performance. (b) Charge-discharge profiles of at various rates NVP-Ti$_{0.15}$/C. (c) Cycling capability tested at 10 C. (d) cycling capability of NVP-Ti$_{0.15}$/C tested at 10 C.

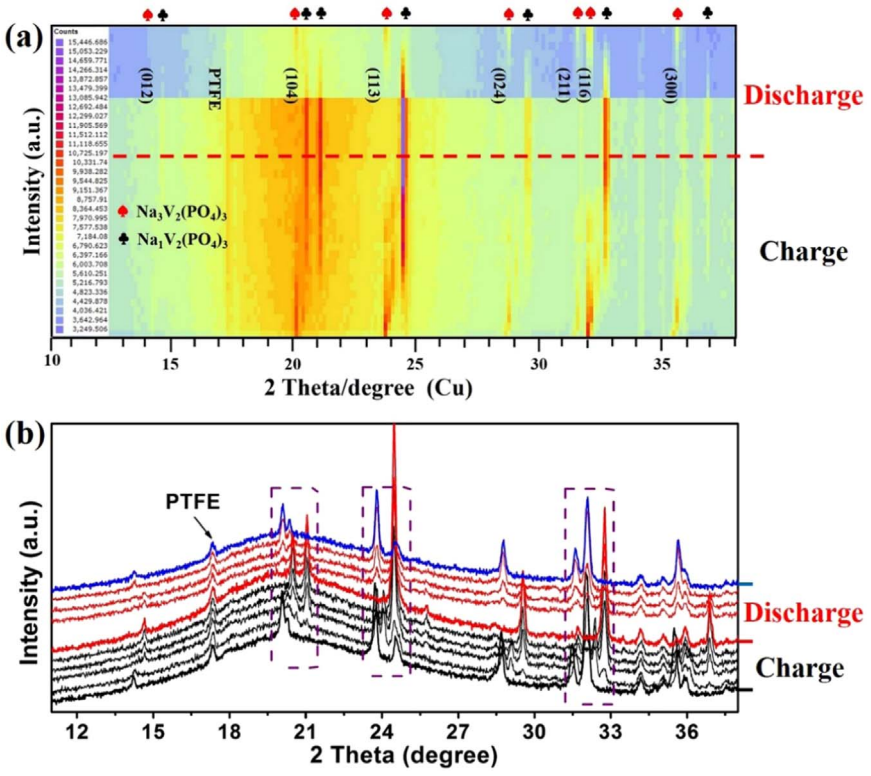


Fig. 5. (a) Contour plots of operando XRD results of NVP-Ti$_{0.15}$/C. (b) Partial operando XRD patterns of NVP-Ti$_{0.15}$/C.

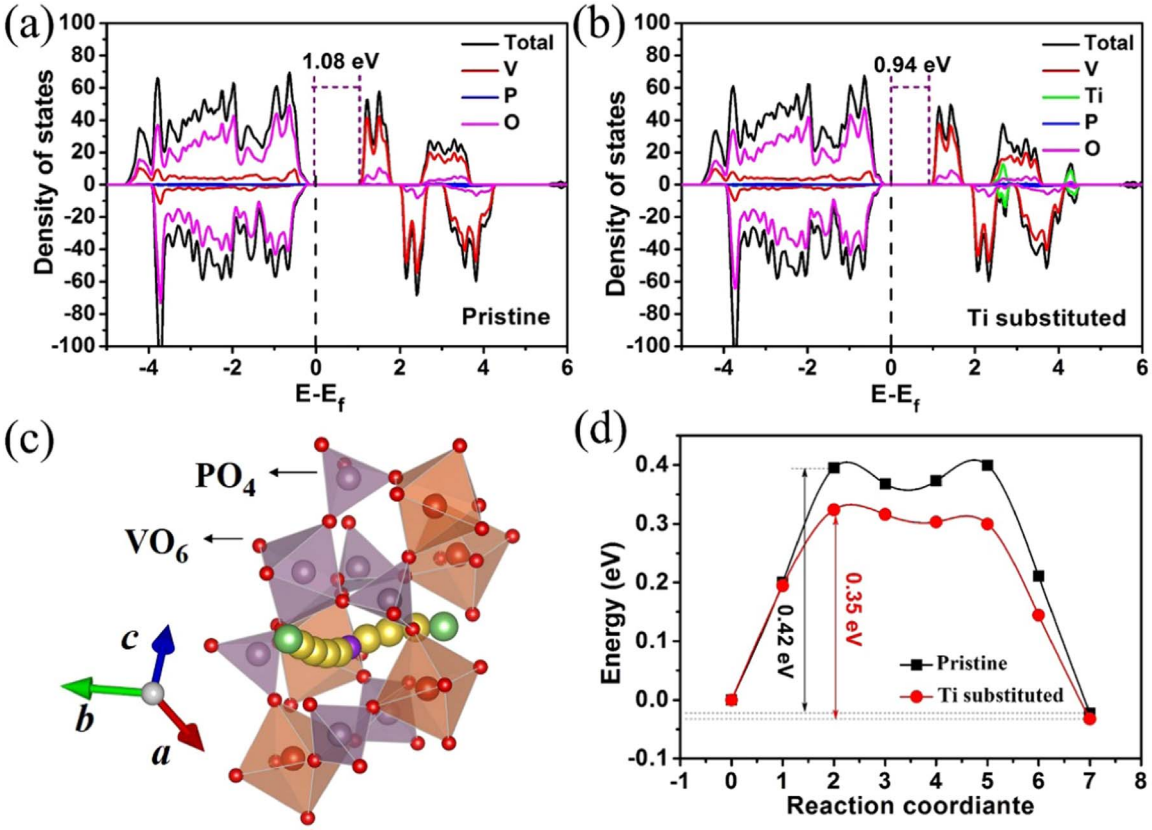


Fig. 6. The density of states: (a) NVP; (b) Ti-substituted NVP. (c) The calculated diffusion trajectory of Na ion along the intra-layer pathway in NVP and (d) the corresponding migration activation energy in NVP and Ti-substituted NVP.

$Na_3V_2(PO_4)_3$ at the end of discharge. Upon sodium insertion/extraction, the peaks shift for $Na_{2.85}V_{1.85}Ti_{0.15}(PO_4)_3$ is lower than that for $Na_3V_2(PO_4)_3$ (Figure S13), demonstrating that the volume change from $Na_{2.85}V_{1.85}Ti_{0.15}(PO_4)_3$ to $NaV_{1.85}Ti_{0.15}(PO_4)_3$ is not so obvious. The smaller volume change is favorable for cycle stability, especially at high temperature.

We carried out first-principle calculations to explore the effects of substitution on intrinsic electronic conductivity and Na ions migration energy barrier. As seen from the projected DOS of pristine and Ti-substituted samples in Fig. 6a and b, the states at low-energy regions are mainly contributed by 2p states of O atoms, while those at high-energy regions are dominated by 3d states of V atoms. The calculated band gap is ~ 1.08 eV, which agrees with previous report [28]. When Ti ions are introduced, the overall DOS of NVP does not change except for the downshift of the conduction band, demonstrating the improved electronic conductivity.

Furthermore, we also observe the effects of vacancies on electronic conductivity (Figure S14). When Na vacancies are introduced, one of the V atoms would change its oxidation state from V^{3+} to V^{4+}, resulting in the formation of a small polaron and hence the enhancement of intrinsic electronic conductivity. The synergistic effect of doping and vacancy gives rise to enhanced conductivity and thus contributes to the high-rate capability. In order to figure out the effect of Ti substituting on ionic conduction, the Na ion diffusion barriers along the intra-layer pathway were calculated. Fig. 6c displays the Na ions diffusion pathway along Na1-Na2-Na1, where a Na ion would migrate through the hexagonal bottleneck of VO_6 octahedra and PO_4 tetrahedra. As plotted in Fig. 6d, the Na ions migrate energy barrier in NVP is 420 meV, whereas the barrier in Ti-substituted material is reduced to 350 meV, which definitely confirms the improved Na ions diffusion by Ti substituting. This can be ascribed to the distance shrinkage of Na2-Na1 and the expansion of Na ion migrate channel after Ti substitution.

4. Conclusion

In summary, a series of Ti substituted NVP-Ti_x/C ($0 \le x \le 0.2$) have been successfully prepared by a facile solid-state reaction method. The XRD and PDF characterizations reveal that Ti substitution does not change the crystal framework of parent material in the doping range of $0 \le x \le 0.2$ but arouses local structure distortion with a shrink of the crystal lattice. DFT calculations show that the energy barriers of Na-ions migration in the Ti-substituted materials are lower than that in NVP. The Ti substitution significantly enhances the reaction kinetics, structure stability and electrochemical performance of NVP/C. NVP-$Ti_{0.15}$/C shows the best cycling stability (a capacity retention of 62% after 2000 cycles at 10 C) and rate capability (70.8 mAh g^{-1} at a high rate of 20 C); it also exhibits outstanding property even at high temperature of 60 °C. Confirmed by operando XRD measurement, the reversible volume change during cycling for Ti-substituted materials is smaller than that of NVP, thus leading to an excellent cycling performance at both room and high temperature. We believe that such structure modification strategy is applicable for developing high-performance NASCON-type cathodes for practical application of SIBs.

Acknowledgments

This work is supported by the National High-Tech R & D Program of China (No. 2016YFB010030X, and 2016YFB0700600), the National Natural Science Foundation of China (No. 51632001) and the project of Innovative Group of Guangdong Province (Grant No. 2014ZT05N013). The authors also thank the State Key Laboratory of Material Processing and Die & Mould Technology and the Analytical and Testing Center of Huazhong University of Science Technology.

Appendix A. Supplementary material

Supplementary data associated with this article can be found in the online version at doi:10.1016/j.ensm.2018.03.021.

References

[1] N. Yabuuchi, M. Kajiyama, J. Iwatate, H. Nishikawa, S. Hitomi, R. Okuyama, R. Usui, Y. Yamada, S. Komaba, Nat. Mater. 11 (2012) 512–517.
[2] C.J. Chen, Y.W. Wen, X.L. Hu, X.L. Ji, M.Y. Yan, L.Q. Mai, P. Hu, B. Shan, Y.H. Huang, Nat. Commun. 6 (2015) 6929–6937.
[3] Y.Y. Huang, X. Li, J.H. Luo, K. Wang, Q. Zhang, Y.G. Qiu, S.X. Sun, S.T. Liu, J.T. Han, Y.H. Huang, ACS Appl. Mater. Interfaces 9 (2017) 8696–8703.
[4] C. Fang, Y. Huang, L.X. Yuan, Y.J. Liu, W.L. Chen, Y.Y. Huang, K.Y. Chen, J.T. Han, Q.J. Liu, Y.H. Huang, Angew. Chem. Int. Ed. 129 (2017) 1–6.
[5] X. Ou, C. Yang, X. Xiong, F. Zheng, Q. Pan, C. Jin, M. Liu, K. Huang, Adv. Funct. Mater. 27 (2017) (1606242-n/a).
[6] X. Xiong, C. Yang, G. Wang, Y. Lin, X. Ou, J.-H. Wang, B. Zhao, M. Liu, Z. Lin, K. Huang, Energy Environ. Sci. 10 (2017) 1757–1763.
[7] M.D. Slater, D. Kim, E. Lee, C.S. Johnson, Adv. Funct. Mater. 23 (2012) 947–958.
[8] L. Wang, Y.H. Lu, J. Liu, M.W. Xu, J.G. Cheng, D.W. Zhang, John B. Goodenough, Angew. Chem. Int. Ed. 52 (2013) 1964–1967.
[9] W. Luo, F. Shen, C. Bommier, H.L. Zhu, X.L. Ji, L.B. Hu, ACC. Chem. Res. 49 (2016) 231–240.
[10] J.-Y. Hwang, S.-T. Myung, Y.-K. Sun, Chem. Soc. Rev. 46 (2017) 3529–3614.
[11] D. Yuan, X. Liang, L. Wu, Y. Cao, X. Ai, J. Feng, H. Yang, Adv. Mater. 26 (2014) 6301–6306.
[12] H. Su, S. Jaffer, H. Yu, Energy Storage Mater. 5 (2016) 116–131.
[13] J.-Y. Hwang, S.-T. Myung, J.U. Choi, C.S. Yoon, H. Yashiro, Y.-K. Sun, J. Mater. Chem. A 5 (2017) 23671–23680.
[14] J.-Y. Hwang, S.-T. Myung, C.S. Yoon, S.-S. Kim, D. Aurbach, Y.-K. Sun, Adv. Funct. Mater. 26 (2016) 8083–8093.
[15] S.-M. Oh, S.-T. Myung, J.-Y. Hwang, B. Scrosati, K. Amine, Y.-K. Sun, Chem. Mater. 26 (2014) 6165–6171.
[16] C.-Y. Yu, J.-S. Park, H.-G. Jung, K.-Y. Chung, D. Aurbach, Y.-K. Sun, S.-T. Myung, Energy Environ. Sci. 8 (2015) 2019–2026.
[17] Z. Jian, W. Han, X. Lu, H. Yang, Y.-S. Hu, J. Zhou, Z. Zhou, J. Li, W. Chen, D. Chen, L. Chen, Adv. Energy Mater. 3 (2013) 156–160.
[18] Y.H. Jung, C.H. Lim, D.K. Kim, J. Mater. Chem. A 1 (2013) 11350–11354.
[19] K. Saravanan, C.W. Mason, A. Rudola, K.H. Wong, P. Balaya, Adv. Energy Mater. 3 (2013) 444–450.
[20] W. Song, X. Ji, Z. Wu, Y. Zhu, Y. Yang, J. Chen, M. Jing, F. Li, C.E. Banks, J. Mater. Chem. A 2 (2014) 5358–5362.
[21] X. Liang, X. Ou, F. Zheng, Q. Pan, X. Xiong, R. Hu, C. Yang, M. Liu, ACS Appl. Mater. Interfaces 9 (2017) 13151–13162.
[22] X. Ou, X. Liang, C. Yang, H. Dai, F. Zheng, P. Wu, Q. Pan, X. Xiong, M. Liu, Energy Storage Mater. 12 (2018) 153–160.
[23] Q. Zhang, W. Wang, Y. Wang, P. Feng, K. Wang, S. Cheng, K. Jiang, Nano Energy 20 (2016) 11–19.
[24] C. Zhu, P. Kopold, P.A. van Aken, J. Maier, Y. Yu, Adv. Mater. 28 (2016) 2409–2416.
[25] F. Lalère, V. Seznec, M. Courty, R. David, J.N. Chotard, C. Masquelier, J. Mater. Chem. A 3 (2015) 16198–16205.
[26] W. Shen, H. Li, C. Wang, Z. Li, Q. Xu, H. Liu, Y. Wang, J. Mater. Chem. A 3 (2015) 15190–15201.
[27] H. Li, Y. Bai, F. Wu, Q. Ni, C. Wu, ACS Appl. Mater. Interfaces 8 (2016) 27779–27787.
[28] K.M. Bui, V.A. Dinh, S. Okada, T. Ohno, Phys. Chem. Chem. Phys. 17 (2015) 30433–30439.
[29] X. Sun, Y. Jin, C.-Y. Zhang, J.-W. Wen, Y. Shao, Y. Zang, C.-H. Chen, J. Mater. Chem. A 2 (2014) 17268–17271.
[30] H. Yoshida, N. Yabuuchi, K. Kubota, I. Ikeuchi, A. Garsuch, M. Schulz-Dobrick, S. Komaba, Chem. Commun. 50 (2014) 3677–3680.
[31] B.H. Toby, J. Appl. Cryst. 34 (2001) 210–213.
[32] G. Kresse, J. Hafner, Phys. Rev. B 49 (1994) 14251–14269.
[33] G. Kresse, Phys. Rev. B 54 (1996) 11169–11186.
[34] P.E. Blochl, Phys. Rev. B 50 (1994) 17953–17979.
[35] J.P. Perdew, K. Burke, M. Ernzerhof, Phys. Rev. Lett. 77 (1996) 3865–3868.
[36] W.W. Kohn, L.J. Sham, Phys. Rev. 140 (1965) A1133–A1138.
[37] H.J. Monkhorst, J.D. Pack, Phys. Rev. B 13 (1976) 5188–5192.
[38] G. Henkelman, H. Jónsson, J. Chem. Phys. 113 (2000) 9978–9985.
[39] J.-N. Chotard, G. Rousse, R. David, O. Mentré, M. Courty, C. Masquelier, Chem. Mater. 27 (2015) 5982–5987.
[40] S.-J. Lim, D.-W. Han, D.-H. Nam, K.-S. Hong, J.-Y. Eom, W.-H. Ryu, H.-S. Kwon, J. Mater. Chem. A 2 (2014) 19623–19632.
[41] A.R. Cho, J.N. Son, V. Aravindan, H. Kim, K.S. Kang, W.S. Yoon, W.S. Kime, Y.S. Lee, J. Mater. Chem. A 22 (2012) 6556–6560.
[42] H.B. Shu, X.Y. Wang, W.C. Wen, Q.Q. Liang, X.K. Yang, Q.L. Wei, B.N. Hu, L. Liu, X. Liu, Y.F. Song, M. Zho, Y.S. Bai, L.L. Jiang, M.F. Chen, S.Y. Yang, J.L. Tan, Y.Q. Liao, H.M. Jiang, Electrochim. Acta 89 (2013) 479–487.
[43] E. Talaie, V. Duffort, H.L. Smith, B. Fultz, L.F. Nazar, Energy Environ. Sci. 8 (2015) 2512–2523.
[44] Y.Y. Hu, Z.G. Liu, K.W. Nam, O.J. Borkiewicz, J. Cheng, X. Hua, M.T. Dunstan, X.Q. Yu, K.M. Wiaderek, L.S. Du, K.W. Chapman, P.J. Chupas, X.Q. Yang, C.P. Grey, Nat. Mater. 12 (2013) 1130–1136.
[45] Y. Jiang, Z. Yang, W. Li, L. Zeng, F. Pan, M. Wang, X. Wei, G. Hu, L. Gu, Y. Yu, Adv. Energy Mater. 5 (2015) 1402104.
[46] W. Duan, Z. Zhu, H. Li, Z. Hu, K. Zhang, F. Cheng, J. Chen, J. Mater. Chem. A 2 (2014) 8668–8675.
[47] F. Omenya, N.A. Chernova, R. Zhang, J. Fang, Y. Huang, F. Cohen, N. Dobrzynski, S. Senanayake, W. Xu, M.S. Whittingham, Chem. Mater. 25 (2013) 85–89.
[48] F. Omenya, B. Wen, J. Fang, R. Zhang, Q. Wang, N.A. Chernova, J. Schneider-Haefner, F. Cosandey, M.S. Whittingham, Adv. Energy Mater. 5 (2015) 1401204.
[49] M.J. Aragon, P. Lavela, G.F. Ortiz, J.L. Tirado, J. Electrochem. Soc. 162 (2015) A3077–A3083.
[50] Z. Jian, C. Yuan, W. Han, X. Lu, L. Gu, X. Xi, Y.-S. Hu, H. Li, W. Chen, D. Chen, Y. Ikuhara, L. Chen, Adv. Funct. Mater. 24 (2014) 4265–4272.